Title

T cells use distinct topographical and membrane receptor scanning strategies that individually coalesce during receptor recognition

Journal

Proceedings of the National Academy of Sciences of the United States of America, 119(32)

ISSN

0027-8424

Authors

Cai, En
Beppler, Casey
Eichorst, John
et al.

Publication Date

2022-08-09

DOI

10.1073/pnas.2203247119

Peer reviewed

PNAS RESEARCH ARTICLE | IMMUNOLOGY AND INFLAMMATION

T cells use distinct topographical and membrane receptor scanning strategies that individually coalesce during receptor recognition

En Cai[a], Casey Beppler[a], John Eichorst[a,b], Kyle Marchuk[a,b,c], Scott W. Eastman[d], and Matthew F. Krummel[a,c,1]

Edited by Michael Dustin, University of Oxford, Oxford, United Kingdom; received February 28, 2022; accepted June 22, 2022

During immune surveillance, CD8 T cells scan the surface of antigen-presenting cells using dynamic microvillar palpation and movements as well as by having their receptors preconcentrated into patches. Here, we use real-time lattice light-sheet microscopy to demonstrate the independence of microvillar and membrane receptor patch scanning. While T cell receptor (TCR) patches can distribute to microvilli, they do so stochastically and not preferentially as for other receptors such as CD62L. The distinctness of TCR patch movement from microvillar movement extends to many other receptors that form patches that also scan independent of the TCR. An exception to this is the CD8 coreceptor which largely comigrates in patches that overlap with or are closely adjacent to those containing TCRs. Microvilli that assemble into a synapse contain various arrays of the engaged patches, notably of TCRs and the inhibitory receptor PD-1, creating a pastiche of occupancies that vary from microvillar contact to contact. In summary, this work demonstrates that localization of receptor patches within the membrane and on microvillar projections is random prior to antigen detection and that such random variation may play into the generation of many individually composed receptor patch compositions at a single synapse.

T cell | microvilli | T cell receptor | synapse

Significance

Motile T cell microvilli palpate surfaces to facilitate surface scanning in a pattern that is independent of the movement of preformed patches of transmembrane antigen receptors across those microvilli. This represents two distinct and parallel surveillance processes: one achieved by topographical scanning and one by membrane scanning across the topography. Once T cell receptors engage, the microvilli act to scaffold multiple receptors within a microvillar close contact.

As a key component of adaptive immunity, T cells continuously survey the surfaces of antigen-presenting cells (APCs) through close membrane contact to detect agonist antigens with high sensitivity. T cell signaling is initiated when the T cell receptor (TCR) complex recognizes its cognate peptide bound to the major histocompatibility complex (pMHC) (1, 2). During T cell activation, a T cell undergoes profound spatial reorganization of its membrane, surface receptors, and downstream signaling molecules to form the immunological synapse (IS), a corrugated membrane apposition to the APC which is critical for T cell signaling and functioning (3, 4).

Given the time constraint for T cells to interact with APCs—the whole-cell contact half-life in vivo is about 1 min (5)—they are highly efficient in antigen detection. Recent evidence suggests that T cell membrane microvilli facilitate T cell antigen search by participating in serial and parallel palpation events that each have a half-life on the order of just a few seconds (6). Upon pMHC recognition, TCR-enriched microvilli (6), visible as "microclusters" (7, 8), are "stabilized" with half-lives that are two to five times that of unengaged "scanning" microvilli (6). Microvillar tips are presumed to facilitate TCR–pMHC binding both because they approach APCs to within 15 nm (6), which is the approximate transmembrane–transmembrane dimension of TCR–pMHC complexes (9, 10), and because TCRs are observed to accumulate in these zones of close contact in response to normal ligand recognition (6, 11).

Biochemical studies demonstrate that TCR half-life for pMHC is a determinant of initiation of TCR signaling; agonism and profound signaling typically require TCR–pMHC half-lives exceeding 4 to 6 s (12). Likewise, initiation of TCR-mediated signaling events occur within seconds of TCR interaction with cognate antigen (13). TCRs appear to reside in preassembled patches or "protein islands," into which other molecules can enter with timescales on the order of seconds, following receptor engagement (14).

These rapid timescales raise the question of how movements of the surface topography (seconds to minutes) and molecular scanning (seconds) are linked, and how and when these are paired during detection and subsequent microvillar stabilization. Further, beyond the TCR, additional membrane receptor–ligand pairs play important roles in enhancing T cell activation and signaling. This includes coreceptor CD8 or CD4 which also binds to MHCs, and both concentrate them (15, 16) and recruit activating lck kinases to the TCR complex (17). Adhesion receptor binding, such as LFA-1 to

Author affiliations: [a]Department of Pathology, University of California, San Francisco, CA 94143-0511; [b]Biological Imaging Development CoLab, University of California, San Francisco, CA 94143-0511; [c]ImmunoX Initiative, University of California, San Francisco, CA 94143-0511; and [d]Lilly Research Laboratories, Eli Lilly and Company, New York, NY 10016

Author contributions: E.C., K.M., and M.F.K. designed research; E.C., C.B., J.E., K.M., and M.F.K. performed research; S.W.E. contributed new reagents/analytic tools; E.C., C.B., J.E., and M.F.K. analyzed data; and E.C., C.B., and M.F.K. wrote the paper.

The authors declare no competing interest.

This article is a PNAS Direct Submission.

[1]To whom correspondence may be addressed. Email: matthew.krummel@ucsf.edu.

This article contains supporting information online at http://www.pnas.org/lookup/suppl/doi:10.1073/pnas.2203247119/-/DCSupplemental.

Published August 1, 2022.

ICAM-1, initiates cell–cell adhesion (18), and later concentrates in the peripheral-supramolecular activation cluster (p-SMAC) of the IS after T cell activation (3). CD28 binds to B7 molecules and generates a critical signal for the activation of naïve T cells, whereas the T cell–surface receptor PD-1 is a major coinhibitory molecule (19).

Evidence shows that most T cell–surface receptors, like the TCR, can also exist in preorganized nanoclusters or protein islands before T cell engagement with pMHC (14). However, most of these previous studies were restricted to either a two-dimensional surface or a thin layer of the T cell, lacking the full three-dimensional (3D) view of the entire T cell membrane. Therefore, it is also unclear how various receptors are distributed prior to T cell activation, and how they behave in comparison with the microvillar structures that bring T cells into close apposition where ligands can bind.

In this work, we used lattice light-sheet microscopy (LLSM) (20) to visualize TCR distribution and membrane topography on entire effector CD8 T cells in three dimensions in real time. This method provided the ability to track both microvilli and receptors and notably receptor patches at high spatial and temporal resolution. We complemented this with a supported bilayer-based method, called synaptic contact mapping (SCM) (6), in which quantum dots (Qdots), whose diameter is bigger than that of TCR–pMHC complexes, are seeded into bilayers containing TCR ligands to enable likewise visualization of the tips of microvilli along with Total Internal Reflection Fluorescence (TIRF)–level measurement of the receptor patches that occupy those contacts. The results demonstrate the independence of membrane topographical scanning and receptor patch scanning and emphasize the heterogeneity of the many isolated signaling patches that, in T cells, are arrayed into distinct spatial regions.

Results

T Cell Receptors Form High-Density Patches and Distribute Independent of Microvilli. To establish a baseline for simultaneous studies of receptor patchiness, patch behavior, and microvillar behavior in three dimensions in real time, we applied LLSM to mouse OT-I T cells. These were surface-labeled with both nonstimulatory antibodies to the highly abundant surface molecule CD45 and nonstimulatory antibodies to the TCRαβ subunits. Full-cell data were assembled by collecting 150 scans of the light sheet at 175-nm z intervals and 0.21-Hz frame rates. Although we cannot resolve details below ∼0.2 μm, LLSM proved superior to confocal microscopy (*SI Appendix*, Fig. S1) even with deconvolution methods, while those methods were orders of magnitude slower for collection of cell volumes. We also reconfirmed that these detection reagents did not induce or enlarge clusters, by performing identical staining on live T cells at 4 °C followed by fixation at 4 °C (*SI Appendix*, Fig. S2) with indistinguishable results. Labeling at 4 °C captures the bona fide resting state of T cells (21).

With the diffraction-limited resolution of LLSM, both microvilli and local foci of higher TCR density, namely patches, were visualized (Fig. 1*A*). Our results confirmed earlier studies that demonstrate TCRs are nonhomogeneously distributed into high-density patches on the membranes of effector T cells. Analyzing TCR patches relative to the CD45-highlighted membrane topography, we observed that some TCR patches localize to tips of microvilli (Fig. 1*B*); some TCR patches localize to flatter membrane regions (Fig. 1*C*); and some microvilli occur with no TCR patches nearby (Fig. 1*D*).

Not all TCRs are in patches. This could best be visualized with image thresholding (Fig. 1*E*). Following application of consistent intensity thresholds as in Fig. 1*E*, 3D surfaces of patches were rendered in Imaris to allow for the calculation of integrated intensity within high-intensity regions (Fig. 1*F*). We thus compared the fraction of receptors in these patches with the total intensity of the TCR, taking advantage of the very high signal-to-noise ratio of LLSM. This demonstrated that, across a range of cellular staining intensities, ∼26% of TCRs are involved in high-density patches (Fig. 1*F*). We do not believe that these accumulations were due to membrane folding as they were not coincident with higher distributions for other receptors such as CD45 (Fig. 1 *A*–*D*), nor others (see also Fig. 3 below).

TCR distribution in patches was also observed in a human T cell line (Jurkat) and in naïve OT-I T cells (*SI Appendix*, Fig. S2). The latter notably lack detectable microvilli and yet had patchy TCR distributions.

When we measured the size of TCR patches (*SI Appendix*, Fig. S3*A*) as resolved by LLSM, we found that their surface area ranged from below the diffraction limit (*SI Appendix*, Fig. S3*B*) up to 3 μm^2 (Fig. 1*E*). CD45, though denser overall, also had patch-like fluctuations of local intensity and these had similar size distributions (Fig. 1*G*). Further, the intensities of fluorescent signals within both TCR and CD45 patches increased proportionally with increasing patch-surface area, suggesting a uniform molecular density within patches (Fig. 1*H*).

As a control for microvillar occupancy by a receptor, we similarly labeled CD62L, a molecule which has previously been found to exclusively localize to microvilli (22). Unlike TCR, CD62L distributions were predominantly on the tips of protrusions (Fig. 1 *I* and *J*). Comparing colocalization of TCR and CD62L patches, we found that 45% of CD62L patches colocalized with TCR patches (Fig. 1*K*). Viewed reciprocally, only 38% of TCR patches were found to colocalize with CD62L patches.

To visualize the distribution of TCR patches and microvillar curvature across the entire cell surface, we projected the 3D cell surfaces for each (Fig. 1*L*) into 2D images using a radial transformation (Fig. 1*M*). The intense CD45 signal allowed for mapping of surface curvature, and this could be viewed as a color-coded image (surface curvature) or overlaid with TCR intensity as a two-color projection (overlay). Examination of overlaid curvature and TCR projections demonstrated again that only a small fraction of TCR patches overlap with high-curvature regions (microvilli). Similarly, when we calculated local surface curvature at locations of TCR patches, we found only a slight preference for those patches to localize to convex surface regions (*SI Appendix*, Fig. S3*C*). Quantifying TCR patch occupancy by CD45 surface curvature gave ∼1/3 occupancy of microvillar tips with TCR patches (*SI Appendix*, Fig. S3*D*), similar to what was quantified using CD62L to mark microvillar tips.

TCR High-Density Patches Move Independently Relative to Microvilli. A key question was whether these patches were stable or might just be stochastic accumulations and, if they were stable, how they would behave relative to motile microvilli. We thus imaged membrane deformation and the TCR on live OT-I T cells with LLSM at frame rates of 0.21 Hz. We found that TCR distributions and microvilli were both highly dynamic (Movie S1) and, when we tracked the movement of TCR patches and nearby microvilli, we found that TCR patches moved independent of microvilli (Fig. 2 *A* and *B*; in which a TCR "falls off" a moving microvillus; Movie S2*A*).

When tracking trajectories of microvilli and TCR patches, we found that we could define TCR patches that moved independent of microvilli, were transiently associated with

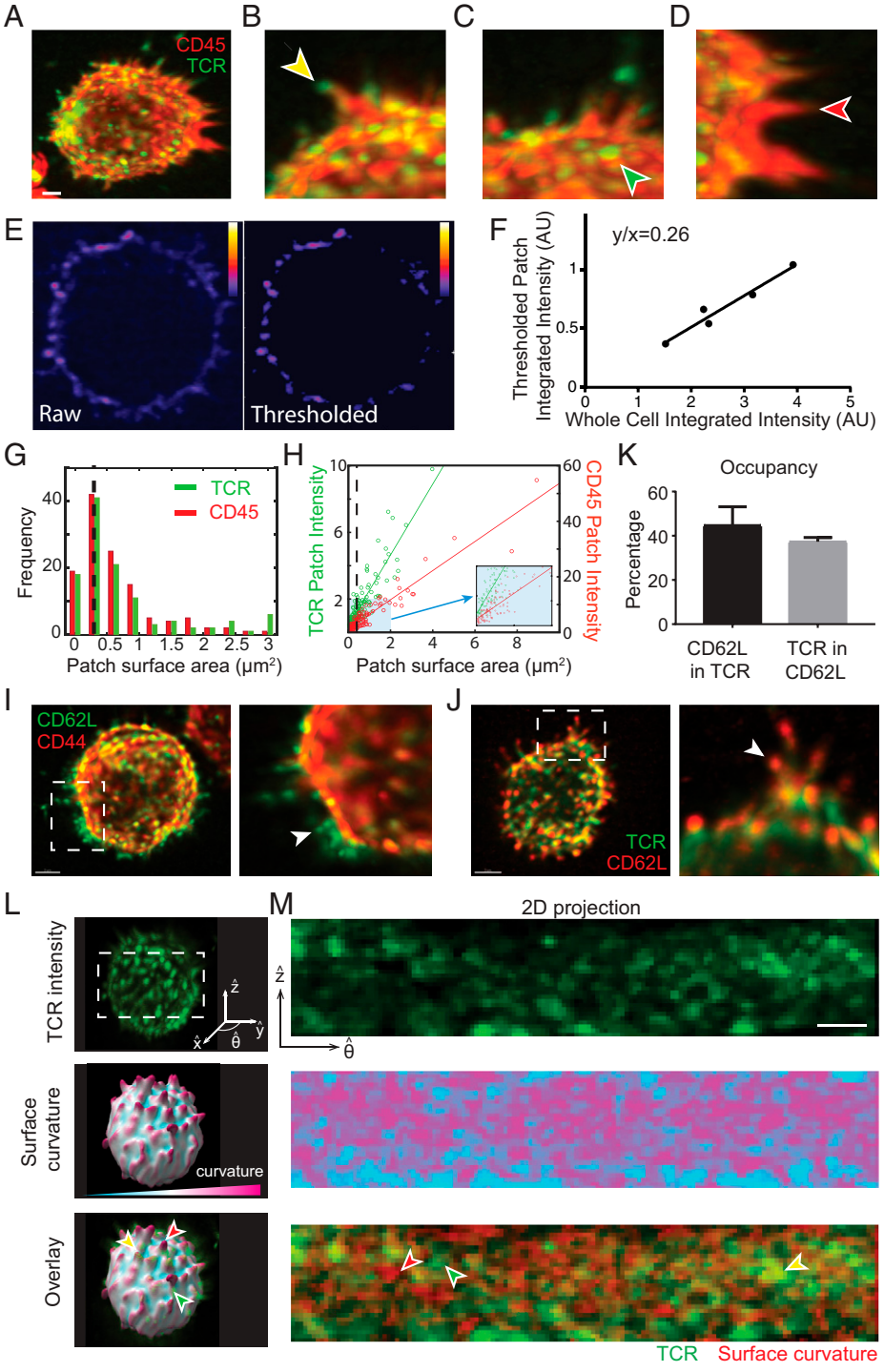

Fig. 1. T cell receptors form high-density patches on previously activated T cells and distribute independent of microvilli. (*A*) LLSM image of a previously activated OT-I T cell stained with fluorescently labeled antibodies against CD45 (anti–CD45-Alexa647) and TCRαβ subunits (H57-Alexa488). The surface staining of TCR and CD45 is rendered in green and red, respectively. (Scale bar, 2 μm.) (*B–D*) Distribution of TCR patches relative to microvilli. Zoomed-in regions show examples of (*B*) TCR patches localized to the tip of a microvillus denoted by the yellow arrow, (*C*) a TCR patch localized outside of microvilli denoted by the green arrow, and (*D*) a microvillus with no TCR patches denoted by the red arrow. (*E*) Slice view of raw (*Left*) and thresholded (*Right*) TCR fluorescence intensity. (*F*) Thresholded data were used to create 3D surfaces, and TCR fluorescence intensity was summed within surfaces to define the thresholded patch integrated intensity where each point shown corresponds to a cell ($n = 5$). (*G*) Size distribution of patches in LLSM on an isolated T cell. The histogram of the patch surface area is obtained from a fixed OT-I T cell stained with fluorescently labeled antibodies against CD45 and TCRαβ subunits. Patch size was determined by using small triangles to cover the edge of the T cell in three dimensions and calculating the sum of the areas of small triangles that constitute the patch. TCR patch sizes are shown in green and CD45 patch sizes are shown in red. The black dashed line shows the patch size at the diffraction limit. (*H*) Patch size and intensity for TCR and CD45 on an isolated T cell. Patch surface area and intensity were measured from the same cell in *G*. Patch surface area and patch fluorescence intensity for TCR and CD45 patches are shown as green dots and red dots, respectively. The black dashed line shows the patch size at the diffraction limit. Solid lines are the linear fitted lines for the data. Fitting for TCR patches has a regression coefficient of 2.13×10^5 with an R^2 of 0.79. Fitting for CD45 patches has a regression coefficient of 5.24×10^5 with an R^2 of 0.89. (*H*, *Inset*) Zoomed-in view of the region in the light blue box. (*I*) Accumulation of CD62L in the microvilli. (*I*, *Left*) LLSM image of an OT-I T cell stained with anti–CD62L-Alexa488 (green) and anti–CD44-Alexa647 (red). (*I*, *Right*) Zoomed-in image of the cell region in the white dashed box. The white arrow points to a microvillus enriched with CD62L. (Scale bar, 2 μm.) (*J*) TCR patches localize independent of microvilli. (*J*, *Left*) LLSM image of an OT-I T cell stained with anti-TCRαβ (H57-Alexa488) and anti–CD62L-Alexa647. (*J*, *Right*) Zoomed-in image of the cell region in the white dashed box. The white arrow points to a microvillus enriched with CD62L but not TCR. (Scale bar, 2 μm.) (*K*) Relationship of TCR and CD62L patches. OT-I T cells ($n = 3$) were stained with anti-TCRαβ (H57-Alexa488) and anti–CD62L-Alexa647 at 4 °C and then fixed at 4 °C. Localizations of 266 CD62L patches over three cells were used to identify microvilli and measure colocalization of 121 TCR patches using a homebuilt algorithm described in *Methods*. Black bar: percentage of CD62L patches that overlapped with TCR patches (error bar: SD). Gray bar: percentage of TCR patches overlayed with CD62L patches (error bar: SD). (*L*) Comparison of TCR patch localization in relation to membrane curvature. T cells from OT-I mTmG mice that express membrane-targeted tdTomato were fixed and then stained with anti-TCRαβ (H57-Alexa488) and anti–CD45-Alexa647. (*L*, *Top*) TCR (green) intensity on the cell membrane in three dimensions. The coordinate system illustrates the vectors used for 2D projection. (*L*, *Middle*) Surface curvature obtained from CD45 intensity data. Local surface curvature is color-coded with a color map showing the relative curvature. A curvature scale bar that is close to binary (cyan: −0.5; magenta: 0.5) is used to indicate protrusions and valleys. (*L*, *Bottom*) Overlay of TCR intensity and surface curvature.The red arrow points to a microvillus with no TCR patches nearby; the green arrow points to a TCR patch on the flatter membrane region and the yellow arrow points to a TCR patch colocalizing with a microvillus. (*M*) Two-dimensional projections of cell volumes from *J*. For ease of visualization, overlay is shown with TCR in green and curvature in red. Arrows denote sites where TCR patches locate on microvilli (yellow) and on flatter membrane regions (green), and where microvilli contain no obvious TCR patches (red). The coordinates show the directions along which the 2D projection was generated from the 3D cell surface. (Scale bar, 2 μm. The pixel size is not uniform in the 2D projection due to morphing. This scale bar is an approximation.)

microvilli, and in rare cases were in prolonged association with a microvillus (Fig. 2 *C* and *D* and Movie S2 *B–D*). We frequently observed cases where TCR patches could be tracked as they moved between microvilli (Fig. 2*D*). Examples of TCR intensities at microvillar tips for each of these forms of interaction are plotted in Fig. 2*E*. Using the tracking data, we

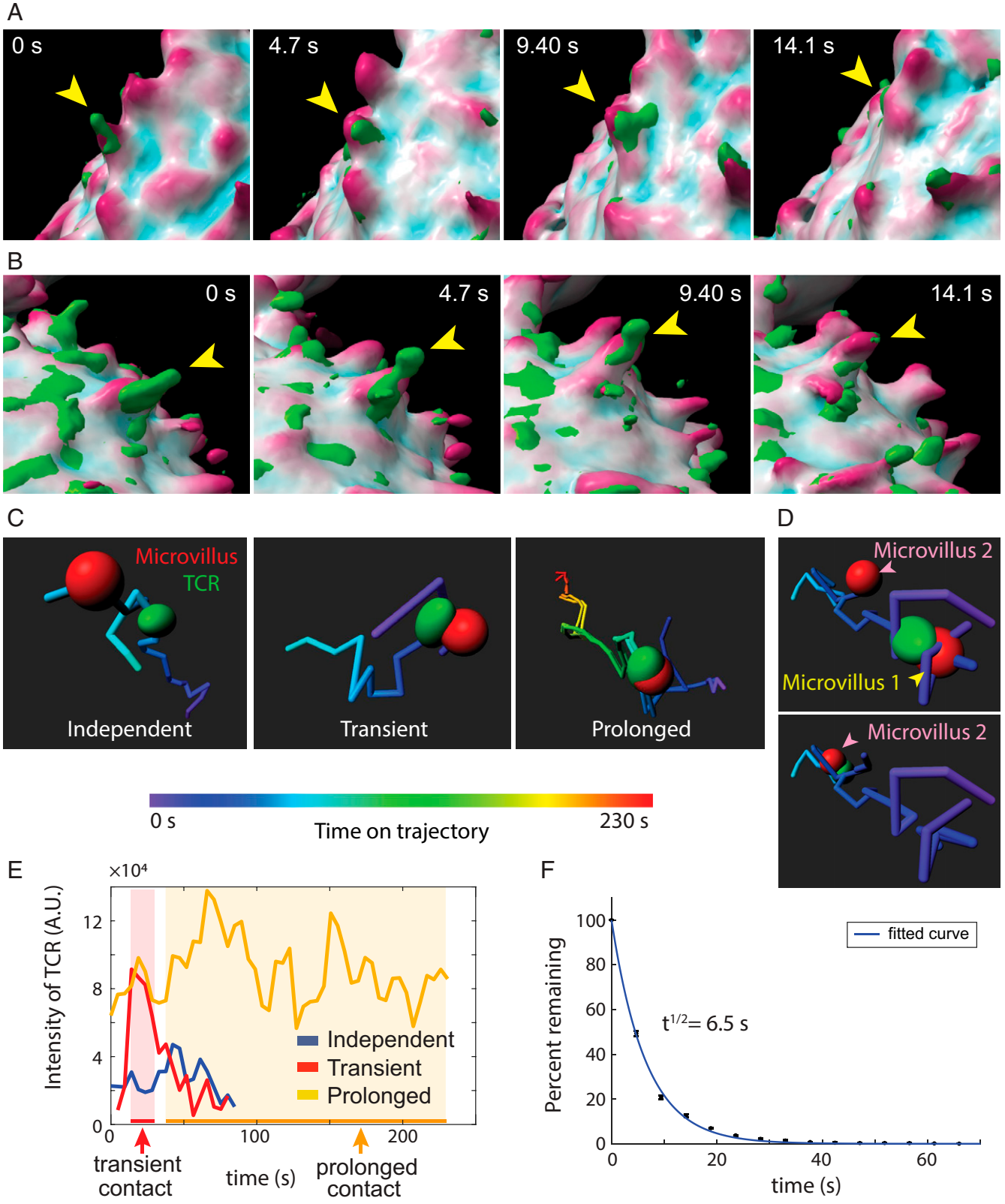

Fig. 2. TCR high-density patches move independently relative to microvilli. (*A*) Time series of a TCR patch (yellow arrows) moving over a microvillus. The T cell surface is rendered based on fluorescent signals of CD45. TCR patches labeled with anti-TCRαβ are shown in green. The surface is color-coded to show the curvature, with cyan showing the concave regions and magenta showing the protrusions. (*B*) Time series of a TCR patch (yellow arrows) transiently interacting with a microvillus during the time course of 14 s. (*C*) Example trajectories of TCR patches that are independently associated (*Left*), transiently associated (*Middle*), or in prolonged association (*Right*) with microvilli. The trajectories are color-coded according to time. Data are extracted from the LLSM movie of a live OT-I T cell stained with anti–CD45-Alexa647 and anti–TCRαβ-Alexa488. TCR patches and microvilli were tracked using the particle tracking function in Imaris. (*D*) The trajectory of a TCR patch that sequentially interacts with two distinct microvilli. (*E*) Fluorescence intensity of TCR patches during interaction with microvilli. Blue: the fluorescence intensity of a TCR patch that is independent of microvilli. Red: the fluorescence intensity of a TCR patch that is transiently associated with a microvillus. Yellow: the fluorescent intensity of a TCR patch that is in prolonged association with a microvillus. (*F*) Decay graph of the association of microvilli with TCR patches. The graph represents TCR patches that have interactions with a microvillus within a 0.5-μm distance (n = 5 cells). Each data point represents the mean ± SEM of the percentage of TCR patches that remain in contact with microvilli at the specific time point.

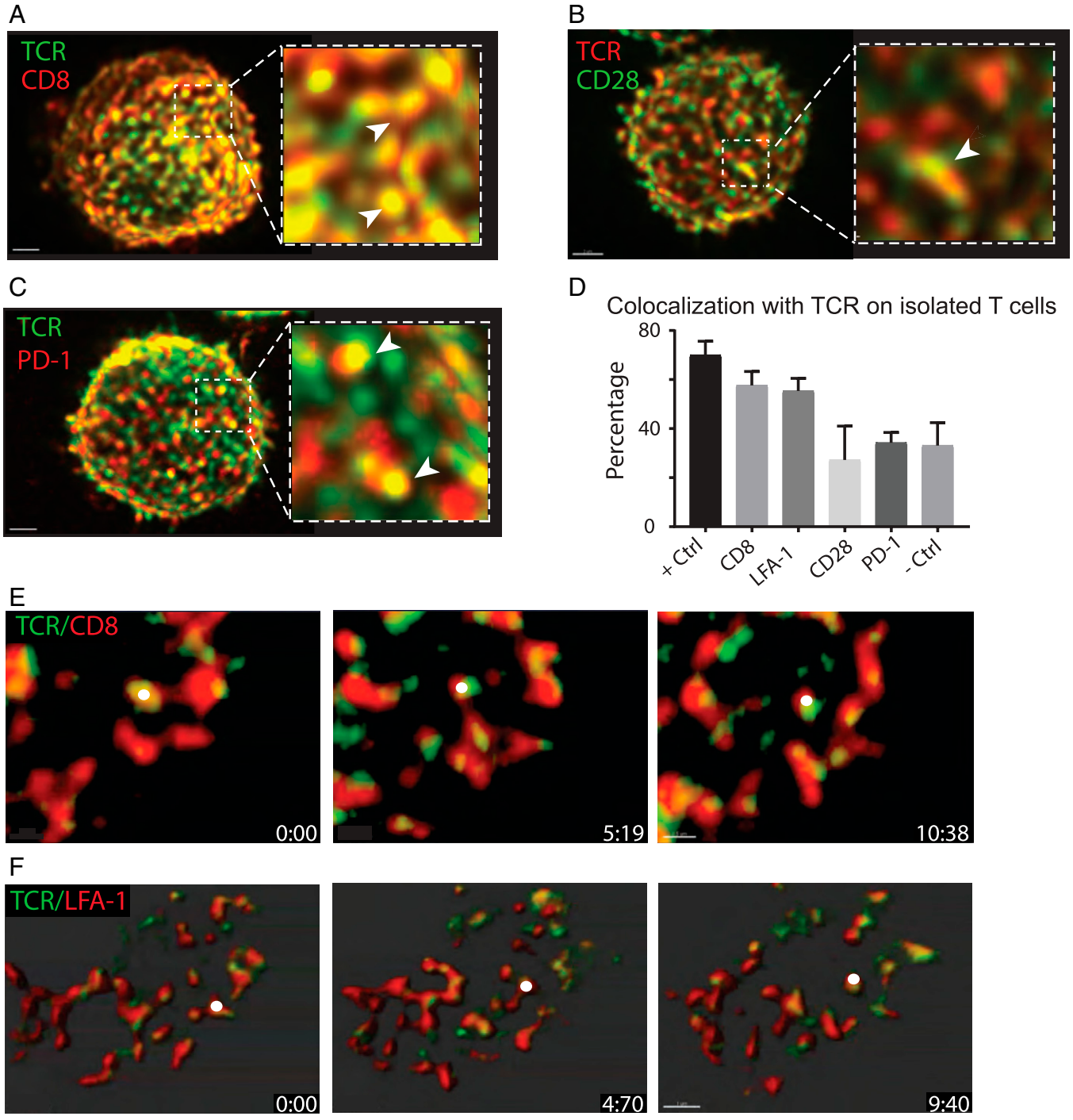

Fig. 3. Independent patch-like distributions of surface receptors relative to TCRs. (*A*) The LLSM image of a fixed OT-I T cell stained with anti–TCR-Alexa488 and anti–CD8-Alexa647. The image shows the front half of the cell to demonstrate the overlap between TCR (green) and CD8 (red). The region in the white box is zoomed-in to show more detail, and the white arrows mark examples of colocalization of CD8 patches (red) with TCR patches (green). (Scale bar, 2 μm.) (*B*) The LLSM image of a fixed OT-I T cell stained with anti–TCR-Alexa488 and anti–CD28-Alexa647. The image shows the front half of the cell to demonstrate the overlap between TCR (red) and CD28 (green). The region in the white box is zoomed-in to show more detail, and the white arrow marks an example of colocalization of CD28 patches with TCR patches. (Scale bar, 2 μm.) (*C*) The LLSM image of a fixed OT-I T cell stained with anti–TCR-Alexa488 and anti–PD-1-Alexa647. The image shows the front half of the cell to demonstrate the overlap between TCR (green) and PD-1 (red). The region in the white box is zoomed-in to show more detail, and the white arrows mark examples of colocalization of PD-1 patches (red) with TCR patches (green). (Scale bar, 2 μm.) (*D*) Percentage of patches colocalizing with TCR patches on isolated T cells for each receptor. Receptor patches are segmented from the surface of the cells and a coreceptor patch with over 20% surface area overlap with a TCR patch is considered as colocalized with the TCR patch. OT-I T cells stained with different clones of antibodies to TCR (H57-Alexa488 and TCR-Vα-Alexa647) are used as positive controls. OT-I T cells stained with antibodies to CD44 and CD62L are used as negative controls. Number of cells used for receptor–TCR colocalization analysis: positive control (n = 2), CD8 (n = 3), CD11a (n = 3), CD28 (n = 2), PD-1 (n = 4), and negative control (n = 5) (error bars: SD). (*E*) Time series of LLSM images of a live OT-I T cell stained with anti–TCR-Alexa488 and anti–CD8-Alexa647. TCRs are shown in green and CD8 patches are shown in red. The white dots denote an example of a CD8 patch that colocalizes and moves with a TCR patch. (Scale bar, 0.5 μm.) (*F*) Time series of LLSM images of a live OT-I T cell stained with anti–TCR-Alexa488 and anti–CD11a-Alexa647. TCRs are shown in green and LFA-1 patches are shown in red. The white dots denote an example of an LFA-1 patch that colocalizes and moves with a TCR patch. (Scale bar, 1 μm.)

calculated the lifetime of the association of these patches with microvilli and found an off-rate ($t^{1/2}$) of about 6 s (Fig. 2*F*), about the amount of time that a microvillus in general dwells in any one region of space. We did not observe coordinated directionality of TCR patch movement relative to each other. These results show that TCR patches dynamically circulate in and out of microvilli during surface scanning, and it is tempting to imagine the membrane as a sort of skin through which some receptors may circulate, as the cytoskeletal ultrastructure moves beneath.

Independent Dynamic Patch-Like Distributions of Coreceptors Relative to TCRs. Using this method, we next sought to compare how other membrane receptors were organized relative to microvilli and TCR patches. To determine the overall distribution and avoid using antibodies under conditions that might alter membrane behaviors, we labeled OT-I T cells at 4 °C with fluorescent antibodies to CD8, CD28, PD-1, and LFA-1 (CD11a) (*SI Appendix*, Fig. S4 *A–D*), in combinations with antibodies to the TCR, akin to what we had done with CD62L (*SI Appendix*, Fig. S4*E*). The OT-I T cells were then fixed at 4 °C for 1 to 2 h.

CD8, the coreceptor, was found in patches and, of the proteins analyzed in this study, was most frequently found near or coincident with TCR patches (Fig. 3 *A* and *D* and *SI Appendix*, Fig. S4*A*). In contrast, CD28 and PD-1 also formed clusters but neither preferentially colocalized with TCR patches in the steady state (Fig. 3 *B–D* and *SI Appendix*, Fig. S4 *C* and *D*). To verify our experimental and analytical procedure for colocalization, we included a positive control experiment in which T cells were labeled with two different clones of antibodies to the TCR, providing a measure of the high end of colocalization (Fig. 3*D*). Comparing across the receptors analyzed, LFA-1 segregated with a propensity to colocalize with the TCR, to a similar extent as CD8 (Fig. 3*D* and *SI Appendix*, Fig. S4*B*). While modestly unexpected because the dimensions of LFA-1–ICAM are longer than those of the TCR, such localization may put LFA-1 in a position to quickly participate in adhesion of a microvillar tip while the TCR serially engages antigens.

With respect to coreceptor CD8 patches, which were frequently found near TCR patches, we then performed live imaging at ∼0.21 Hz, tracking both CD8 and TCR patches with LLSM. This showed that CD8 patches typically were either overlapping or "followed" the movement of TCR patches on isolated OT-I T cells before antigen engagement (Fig. 3*E* and Movie S3). A similar prolonged association was observed for the TCR with LFA-1 (Fig. 3*F* and Movie S4). To compare the dynamics of CD8, LFA-1, and TCR patches, we calculated the mean speed of patches and their mean square displacement (MSD) (*SI Appendix*, Fig. S5). This showed that microvilli and TCR, CD8, and LFA-1 patches moved at speeds close to 5 μm/min (measured at 0.21 frames per second). To determine their diffusion pattern, we fitted the MSD to a power fit ($y = ax^b$). The resulting power coefficients (b) of TCR patches and CD8 patches were 0.99 and 1.04, respectively, suggesting normal diffusion, while the power coefficient of LFA-1 patches was 0.85, suggesting a confined diffusion.

Occupancy and Convergence of TCRs and PD-1 to Microvillar Tips upon Antigen Detection. To study the coassembly of TCR and microvilli after antigen recognition, we first used SCM (6) whose temporal resolution of the contact region is superior to LLSM since all the key data are taken in a single plane. As previously, we incorporated fluorescent Qdots with radii of ∼16 nm into a supported lipid bilayer bearing ligands for T cells (Fig. 4*A*). When T cells made close contact with the bilayer, these fluorescent Qdots were sterically excluded from the contact region, leaving a dark microvillar "footprint" of the contact region (Fig. 4 *A*, *B*, and *G*). This allowed us to track both TCR patches and the nearest microvillar contacts on lipid bilayers at a time resolution between 1 and 2 s.

As previously observed (6), most microvillar contacts did not have profound TCR occupancy in the absence of stimulating ligands as measured here by LLSM (Fig. 1). This number rose to 85.5% when bilayers contained activating pMHCs compared with 25.6% when bilayers contained no activating pMHCs (Fig. 4 *B* and *C*), and previous work has shown that this is dependent on the agonist peptide and not simply the MHC (6). Further, when we quantified the stability of close contacts on stimulating bilayers, we were able to detect a difference in TCR occupancy between those that were short-lived (persistence time shorter than 3 sigma above the average persistence time of TCR^- contacts), persistent (persistence time greater than 3 sigma above the average persistence time of TCR^- contacts), and ultrapersistent (defined here as persistence greater than 90 s). In the same synapse, TCR occupancy in superstable close contacts that had persistence times over 90 s was increased on average 2.9 times compared with transient contacts (Fig. 4*D*).

Finally, we took the example of PD-1 to determine the extent to which receptors of similar dimensions partitioned together in the IS. Imaging this receptor and its ligand in real time in a fluorescent protein-transfected cell system, now using LLSM imaging, we found that PD-1 patches accumulate at the initial contact sites as puncta (Fig. 4*E* and Movie S5) and increase in intensity during synapse formation (Fig. 4*F*), suggesting that more receptors are brought into the same contact, rather than one contact having a fixed amount of receptor.

To observe this in the SCM setting and also track whether TCR patches become inhabited by PD-1, we labeled both receptors on T cells placed onto bilayers containing ICAM-1, activating pMHCs, and recombinant mouse PD-L1 (Fig. 4*G*). After 3 to 5 min of interaction, we found that PD-1 clusters were typically found in Qdot-low regions, indicating that this receptor–ligand pair also accumulates at close contacts and consistent with the length of PD-1–PD-L1 interaction being on the order of 14 nm, shorter than the size of our tethered Qdot. Within these contacts, cells typically had slightly more microvilli that were occupied by the TCR alone, with no detectable PD-1 coclustering as compared with those that were co-occupied by both the TCR and high densities of PD-1 (Fig. 4*H*). This indicates that there is no obligate comigration of these receptors and likely that there is stochastic engagement and assembly of each into a microvillus. To that end, some contacts (∼20%) were $PD\text{-}1^+$ but TCR-low with indistinguishable fractions that were $TCR^+PD\text{-}1^+$ ($P = 0.26$) (Fig. 4*I*). This might again imply stochasticity of PD-1 cluster entry into a microvillar region although more studies will be needed to fully understand this. In sum, we observe that microvillar contacts fill with multiple receptors during recognition.

Discussion

In this study, we demonstrate that on effector T cells prior to antigen engagement, TCRs are distributed into high-density patches. The patch area varies from below the diffraction limit to about 3 μm^2, with most patches sized at or below the diffraction limit (∼0.2 μm^2). This suggests that most TCR patches are nanoscale clusters. This finding is consistent with

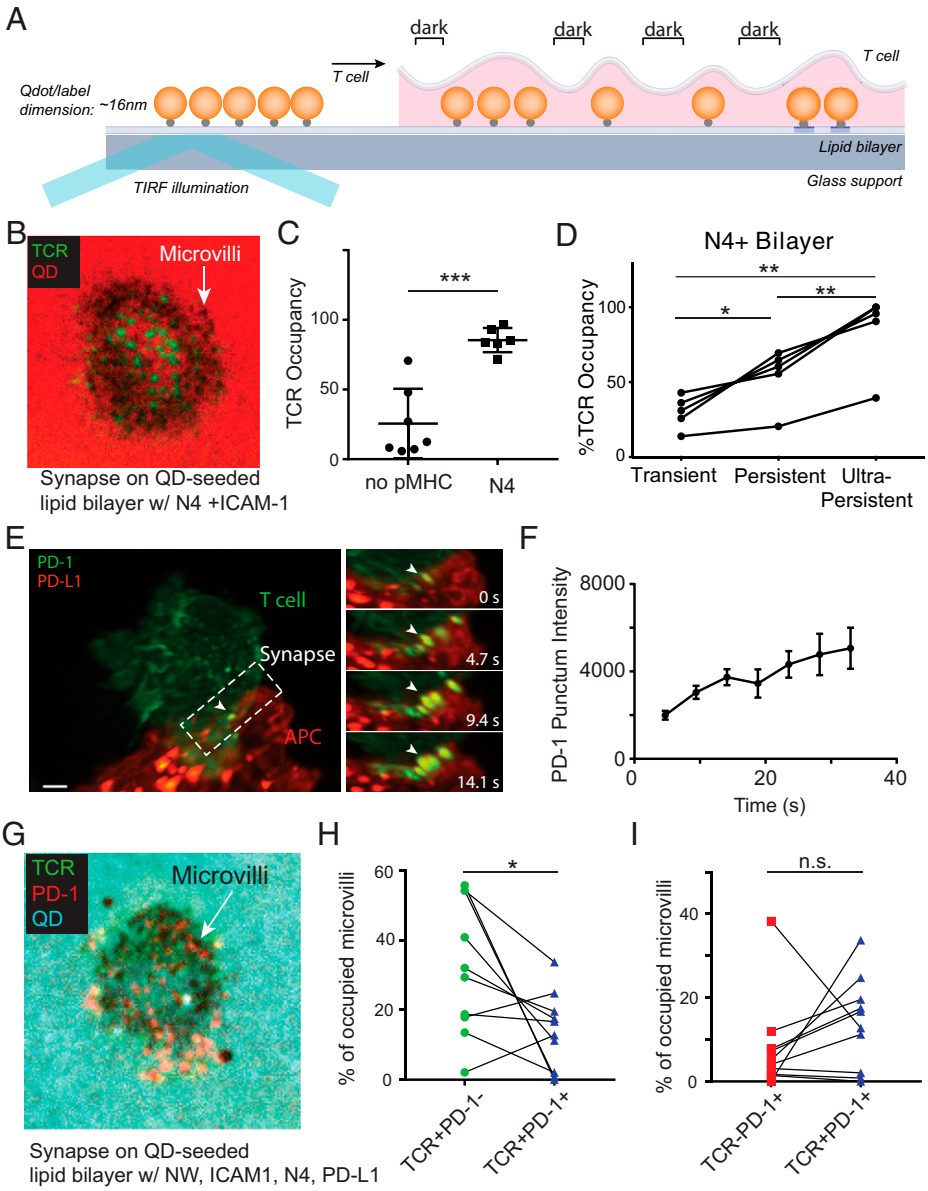

Fig. 4. TCR patches and PD-1 patches converge to microvillar tips upon antigen detection. (*A*) Principle of synaptic contact mapping. Fluorescent Qdot beads of ~16-nm diameter are incorporated into lipid bilayers which are then seeded with ligands for T cells. Qdot exclusion from a region occurs when a microvillus approaches the bilayer, leading to exclusion of Qdots from this region and a "hole" in the otherwise flat fluorescent field formed by the Qdots. (*B*) SCM image of a synapse of an OT-I T cell formed on a lipid bilayer containing ICAM-1 and N4. OT-I T cells are stained with anti–TCR-Alexa488. TCR microclusters are in green; Qdot (QD) signal is in red. Dark spots (as indicated by white arrows) show the locations of microvilli contacting the bilayer where Qdots are sterically excluded. (*C*) TCR occupancy from SCM images for cells interacting with bilayer containing activating N4 pMHC (85.5 ± 3.5% [mean ± SEM], $n = 7$) and cells interacting with bilayer containing no activating N4 pMHC (25.6 ± 9.4% [mean ± SEM], $n = 6$). ***$P = 0.0004$, unpaired t test with Welch's correction. (*D*) TCR occupancy of microvilli on an activating bilayer with N4 pMHC segmented by transient, persistent, and ultrapersistent microvilli. Transient microvillar contacts were defined as contacts with persistence times shorter than 3 sigma above the average persistence time of TCR$^-$ contacts (cutoffs ranging from ≤4 to 10 s between cells). Persistent microvillar contacts were defined as contacts with persistence times greater than 3 sigma above the average persistence time of TCR$^-$ contacts (cutoffs ranging from ≥4 to 10 s between cells). Ultrapersistent microvillar contacts were defined as contacts with persistence time over 90 s. *$P = 0.0229$ for the transient and persistent group, **$P = 0.0034$ for the persistent and ultrapersistent group, and **$P = 0.0019$ for the transient and ultrapersistent group. All statistical comparisons were made using paired t test ($n = 5$). (*E*) PD-1 accumulation at contacts during synapse formation by LLSM. Image of a Jurkat cell genetically expressing PD-1-mNeonGreen (green) interacting with a CHO cell expressing PD-L1-mScarlet (red) and the TCR activator. The synapse region in the white dashed box is zoomed-in and the time series of the region is shown (*Right*). White arrows in each panel mark the same patch of PD-1 at different time points. (Scale bar, 2 μm.) (*F*) Increase of fluorescence intensity of a PD-1 punctum from *E*. PD-1 puncta ($n = 5$) were tracked using Imaris and mean intensity was measured for each punctum over time (error bars: SD). (*G*) SCM image of a synapse of an OT-I T cell formed on a lipid bilayer containing ICAM-1, N4, and PD-L1. TCR signal is shown in green, PD-1 signal is shown in red, and Qdot signal is shown in cyan. Dark spots (as indicated by the white arrow) show the locations of microvilli contacting the bilayer where Qdots are sterically excluded. (*H*) Percentage of microvilli on synapses ($n = 9$) occupied by TCR clusters only (green) and both TCR and PD-1 clusters (blue). *$P = 0.0336$, paired t test. (*I*) Percentage of microvilli on synapses ($n = 9$) occupied by PD-1 clusters only (red) and both TCR and PD-1 clusters (blue). $P = 0.2607$, paired t test. n.s., not significant.

the observation of preorganized TCR nanoclusters or protein islands on nonactivated T cells (14). Interestingly, we observed TCR patches on naïve T cells which have almost no microvilli. This indicates that TCR patch formation is independent of membrane topography. Although TCR patches have a slightly higher probability of locating on membrane protrusions, their localization is not restricted to microvilli. This finding is on its face different from the work of Haran and coworkers which used multiangle TIRF imaging to conclude that the TCR and other receptors are preassembled on microvilli (21, 23). One

explanation for the discrepancy in these studies might be due to calculations made in multiangle TIRF which may underrepresent the relative intensities when moving away from a coverslip and thus underestimate intensities of patches on the cell body. Similar cell preparations and sample preparations appear to be used in both studies although unknown variations in these may also contribute. As noted, although much of the TCR is in these patches which have little microvillar localization, a significant portion of the TCRs also appears distributed throughout the membrane outside of patches and would be easily detected by TIRF methods. A limitation of our work is that we focus upon patches, and it is possible and indeed likely that receptors that are not contained in patches circulate and will also, therefore, populate microvilli, even when no patches are found there. Another limitation of our work is that we do not have the capability with SCM to determine if antigen-dependent TCR microclusters are formed from preexisting patches or from freely diffusing TCRs. It is possible that antigen-dependent TCR microclusters arise from both preexisting patches and from clustering of free diffusing TCRs. Our work clearly demonstrates a distinction between receptors such as CD62L and the TCR, as well as between TCR patches and other receptor patches (e.g., CD8), which are also not obligately associated with microvilli.

In the immune synapse, it is well-established that TCRs aggregate as microclusters and subsequently migrate to the center of the synapse upon engaging antigen (8). Prior to this work, it was known that PD-1 colocalizes with the TCR upon binding to PD-L1 and that PD-1–TCR colocalization is required for PD-1–mediated inhibition of TCR signaling (24). Our study finds similarly, albeit with the provision that there are multitudes of mixed clusters containing more or less of PD-1 or TCR. However, those studies which relied upon TIRF imaging did not have the ability to visualize how coreceptors are distributed relative to TCRs before antigen engagement. Here, we show that, in addition to TCRs, other T cell–surface receptors are also distributed into high-density patches on effector T cells prior to activation. This confirms that TCRs are nonuniformly distributed on T cell membranes.

Our previous work had shown that T cells palpate a bilayer with microvilli that are only sparsely occupied with TCRs. Three-dimensional real-time visualization validates that TCR patches do not obligately live in microvilli, while a control molecule known to preferentially inhabit microvilli, CD62L, was found there, consistent with older work (22). Notably, the coreceptor CD8 often migrates together with the TCR which may specifically enhance its ability to coengage MHC-I molecules on opposing cells. Other receptors, notably CD28 and PD-1, also assemble as patches but do so typically independent of TCR patches.

Like microvilli, TCR patches are highly dynamic. Their movements are not restricted by microvilli: Most TCR patches are only transiently associated with microvilli and frequently move in and out of microvilli. Thus, T cell microvillar dynamics (6) and molecular search are largely independent. This may provide benefits for T cells to be able to use microvilli that contain sparse nonclustered TCRs to discover large depots of pMHCs while microvilli occupied by clustered TCRs could be sensitive to engaging limited collections of pMHCs through serial triggering. Microvilli- and TCR patch–independent movements enable particular microvilli to rapidly switch between TCR-dense and TCR-sparse states, possibly facilitating efficient antigen scanning.

To that end, previous work had demonstrated preclustering of LFA-1 (25) and this integrin has long been known to play an essential role in early T cell synapse formation, binding prominently away from the TCR and subsequently forming an adhesion ring (p-SMAC) while TCRs centralize (3). Our finding that LFA-1 patches frequently colocalize with TCRs provides a needed piece of information that adhesive force from preclustered LFA-1 is often available in extremely close proximity to the TCR patches. In this setting, it is tempting to speculate that recognition of pMHC and rapid local high-avidity LFA-1 interactions can be efficiently temporally linked. Because TCR signaling intermediates can up-regulate LFA-1 affinity via inside-out signaling (26), those integrins may be activated at very low pMHC densities and then assist to stabilize a microvillar contact to permit further TCR signaling. Although signaling downstream of ZAP70 is not required for microvillar stabilization in settings of abundant pMHC (6), it is possible that inside-out signaling to LFA-1 increases the T cell's sensitivity in very low antigen settings. Integrins are thought to ultimately be excluded from close contact and then migrate to the p-SMAC as described.

In summary, this work defines the independence of surface receptor movement and microvillar movement on effector T cells before antigen detection. Future work should be possible to understand how dual topographical/receptor scanning can lead to high sensitivities of receptor recognition.

Methods

Mice. All mice were housed and bred at the University of California, San Francisco, according to Laboratory Animal Resource Center guidelines. Protocols were approved by the Institutional Animal Care and Use Committee of the University of California.

Cell Culture. OT-I T cells were maintained in RPMI supplemented with 10% fetal bovine serum, 100 U/mL penicillin, 0.1 mg/mL streptomycin, 2 mM L-glutamine, 10 mM Hepes, and 50 μM β-mercaptoethanol (complete RPMI). Single-cell suspensions were prepared from the lymph nodes and spleens of OT-I TCR transgenic mice. Splenocytes were incubated in complete RPMI with 100 ng/mL SIINFEKL peptide for 30 min at 37 °C. The splenocytes were washed three times and suspended in media. Lymphocytes and splenocytes were then mixed 1:1 at 2×10^6 total cells per milliliter, and 30 mL of the cell mix was transferred to a T75 flask. After 48 h, 30 mL of media with interleukin-2 (IL-2) was added to the flask (final concentration of IL-2: 10 U/mL). After 72 h, cells were removed from the flask, spun down, and resuspended in fresh media with IL-2 and held in culture for an additional 48 to 96 h before use.

Bone marrow dendritic cells (BMDCs) were maintained in Iscove's Modified Dulbecco's Medium (IMDM) supplemented with 10% fetal bovine serum, 100 U/mL penicillin, 0.1 mg/mL streptomycin, 2 mM L-glutamine, and 50 μM β-mercaptoethanol (complete IMDM). BMDCs were prepared from the bone marrow of C57BL/6 mice. BMDCs were incubated in complete IMDM supplemented with 20 ng/mL granulocyte–macrophage colony-stimulating factor (GM-CSF) for 6 to 10 d. Fresh IMDM and GM-CSF were replenished every 48 h and cells were passaged on day 5 and day 9. BMDCs were then treated with 60 ng/mL recombinant murine IL-4 for 2 to 3 d before planned usage and matured using 1 μg/mL lipopolysaccharide for 5 h to overnight before use.

Jurkat-NFAT-PD-1-mNeonGreen cells and CHO-TCRact-PD-L1-mScarlet were from Eli Lilly and Company and described previously. Briefly, CHO-TCRact-PD-L1-mScarlet cells were generated by transduction of CHO-TCRact cells (Promega, J1191: aAPC/CHO-K1) with virus from pLVX-PD-L1-mScarlet lentiviral vector (synthesized by GenScript) and cultured in F12 supplemented with 10% fetal bovine serum, 200 mg/mL hygromycin B, and 500 mg/mL G418. CHO-TCRact-PD-L1-mScarlet cells were passaged when the density reached 80 to 90% confluency. Jurkat-NFAT-PD-1-mNeonGreen suspension cells were generated by transduction of Jurkat-NFAT cells (Promega, CS176401) with virus from LVX-PD-1-mNeonGreen lentiviral vector (synthesized by GenScript) and cultured in RPMI1640 supplemented with 10% fetal bovine serum, 200 mg/mL hygromycin B, 500 mg/mL G418, 1 mmol/L sodium pyruvate, and 0.1 mmol/L minimum essential medium

nonessential amino acids. Jurkat-NFAT-PD-1-mNeonGreen cells were passaged when the cell suspension density reached 2×10^6 cells per milliliter. Polybrene (Sigma-Aldrich, TR-1003) was used for lentiviral transduction according to the manufacturer's instructions.

Cell Preparation for Imaging. To prepare OT-I T cells for imaging, live cells were harvested using Ficoll-Paque, washed with complete RPMI, and then held at 37 °C. To stain receptors and membranes of T cells for live-cell imaging, 2×10^6 cells were spun down and resuspended in 100 μL RPMI. The cells were then stained with combinations of monoclonal antibodies conjugated to Alexa Fluor dyes on ice for 30 min. Cells were then rinsed once with complete RPMI. In SCM experiments, live cells were imaged in RPMI (without phenol red) supplemented with 2% fetal bovine serum, 100 U/mL penicillin, 0.1 mg/mL streptomycin, 2 mM L-glutamine, 10 mM Hepes, and 50 μM β-mercaptoethanol (imaging media). In LLSM experiments, live cells were imaged in RPMI (without phenol red) supplemented with 10% fetal bovine serum, 100 U/mL penicillin, 0.1 mg/mL streptomycin, 2 mM L-glutamine, 10 mM Hepes, and 50 μM β-mercaptoethanol (imaging media). For TCR staining, 2.5 μg H57-597 nonblocking monoclonal antibody conjugated to either Alexa Fluor 488 or Alexa Fluor 647 was used for 5×10^6 cells. For CD45 staining, 2.5 μg of CD45 nonblocking monoclonal antibody (clone 30-F11) conjugated to either Alexa Fluor 488 or Alexa Fluor 647 was used. For CD8 staining, 2.5 μg of CD8a monoclonal antibody (clone 53-6.7) was conjugated to Alexa Fluor 488. To image PD-1 on OT-I T cells, cells were activated with Dynabeads mouse T activator CD3/CD28 beads for 48 h. This method increased surface PD-1 levels and made it possible to detect. For PD-1 staining, 2.5 μg of PD-1 nonblocking monoclonal antibody (clone RMP1-30) conjugated to Alexa Fluor 647 was used.

In SCM live-cell imaging, 2×10^5 cells were added to the bilayer well. Once cells began interacting with the bilayer, imaging was initiated. To prepare for SCM fixed-cell imaging, 2×10^5 cells were added to the bilayer well. Cells were allowed to interact with the bilayer for 3 to 5 min at 37 °C. Cells were then fixed with 20 mM Hepes, 0.2 M sucrose, 4% paraformaldehyde (PFA), and 0.01% glutaraldehyde for 10 min at 37 °C and washed with phosphate-buffered saline (PBS) before imaging.

To prepare for LLSM live-cell imaging, BMDCs were washed with complete IMDM and plated on fibronectin-coated coverslips 15 min before use. OT-I T cells were harvested using Ficoll-Paque, washed with complete RPMI, and then held at 37 °C. OT-I T cells (2×10^6) were stained with 2.5 μg of CD45 nonblocking monoclonal antibody conjugated to either Alexa Fluor 488 or Alexa Fluor 647 on ice for 30 min, and then rinsed once with complete RPMI. OT-I cells were added to coverslips with BMDCs and incubated for 10 min at 37 °C.

To prepare for LLSM fixed-cell imaging, OT-I T cells were harvested using Ficoll-Paque and washed with complete RPMI. To reduce the possibility of T cell activation due to antibody cross-linking, T cells were labeled and fixed at 4 °C. OT-I T cells (2×10^6) were stained in cold complete RPMI with different combinations of monoclonal antibodies conjugated to Alexa Fluor dyes on ice for 30 min, and then washed with cold PBS with 5 mM ethylenediaminetetraacetic acid (EDTA) at 4 °C three times. Cells were then fixed with 20 mM Hepes, 0.2 M sucrose, 4% PFA, and 0.01% glutaraldehyde on ice for at least 1 h. Fixed cells were washed with cold PBS and spun down on coverslips coated with Cell-Tak (Corning) before imaging. For CD62L staining, 2.5 μg of CD62L monoclonal antibody (clone MEL-14) conjugated to Alexa Fluor 647 was used. For CD11a staining, 2.5 μg of CD11a monoclonal antibody (clone M17/4) conjugated to Alexa Fluor 488 was used. For CD28 staining, 2.5 μg of CD28 monoclonal antibody (clone F28) conjugated to Alexa Fluor 488 was used. Isolated cells were selected for analysis. All antibodies were from BioLegend unless otherwise specified.

Supported Lipid Bilayers. Preparation and use of supported lipid bilayers were as previously described (6, 27). Briefly, phospholipid mixtures consisting of 96.5% 1-palmitoyl-2-oleoyl-glycero-3-phosphocholine (POPC, Avanti Polar Lipids 850457), 2% 1,2-dioleoyl-sn-glycero-3-[(N-(5-amino-1-carboxypentyl)iminodiacetic acid)succinyl] (nickel salt) (DGS-NTA (Ni), Avanti Polar Lipids 790404), 1% 1,2-dioleoyl-sn-glycero-3-phosphoethanolamine-N-(cap biotinyl) (sodium salt) (biotinyl-cap-PE, Avanti Polar Lipids 870273), and 0.5% 1,2-dioleoyl-sn-glycero-3-phosphoethanolamine-N-[methoxy(polyethylene glycol)-5000] (ammonium salt) (PEG5,000-PE, Avanti Polar Lipids 880230) in chloroform were mixed in a round-bottom flask and dried, first under a stream of dry nitrogen and then overnight under vacuum. All phospholipids were products of Avanti Polar Lipids. Crude liposomes were prepared by rehydrating the phospholipid cake at a concentration of 4 mM total phospholipids in PBS for 1 h. Small, unilamellar liposomes were then prepared by extrusion through 100-nm Track-Etch filter papers (Whatman) using a Liposo-Fast extruder (Avestin).

Eight-well Nunc Lab-Tek II chambered coverglasses were emersed in 5% Hellmanex at 55 °C overnight. The chambers were washed repeatedly with 18 MΩ water. After air drying, 250 μL of 3 M NaOH was added to each well and kept at 55 °C for 15 min. The chamber was then washed with 18 MΩ water. This was repeated, and then the chamber was washed repeatedly with 18 MΩ water and dried under a stream of compressed air. Lipid bilayers were set up on a chambered coverglass by adding 0.25 mL of a 0.4 mM liposome solution to the wells. After 30 min, wells were rinsed with 8 mL of PBS by repeated addition of 0.5-mL aliquots, followed by aspiration of 0.5 mL of the overlay, leaving ∼0.25 mL. Nonspecific binding sites were then blocked with 1% bovine serum albumin (BSA) in PBS for 30 min. After blocking, 25 ng of unlabeled streptavidin was added to each well and allowed to bind bilayers for 30 min. After rinsing, protein mixes containing 63 ng ICAM and 6 ng pMHC in 2% BSA were injected into each well. In experiments where TCR and PD-1 localization was imaged, protein mixes containing 63 ng ICAM, 6.25 ng pMHC, and 6.25 ng recombinant mouse PD-L1 with 6-His tag (R&D Systems) in 2% BSA were injected into each well in this step. ICAM preparation was described previously while pMHC was provided by the NIH Tetramer Facility. After binding for 30 min, wells were rinsed again and 25 ng of Qdot-streptavidin was added to each well. Bilayers were finally rinsed with imaging media before being heated to 37 °C for experiments. Imaging media were prepared by supplementing RPMI with 2% fetal bovine serum, 100 U/mL penicillin, 0.1 mg/mL streptomycin, 2 mM L-glutamine, 10 mM Hepes, and 50 μM β-mercaptoethanol.

Lattice Light-Sheet Microscopy. LLSM imaging was performed in a manner previously described. Briefly, for imaging living cells, 5-mm round coverslips were cleaned by a plasma cleaner and coated with 2 μg/mL fibronectin and TetraSpeck fluorescent beads (Invitrogen; 0.1 μm at 1.8×10^8 beads per milliliter) in PBS at room temperature for 1 h or 4 °C overnight before use. TetraSpeck beads were used as fiducial markers for correction of shift between different fluorescent channels. BMDCs were dropped onto the coverslip and incubated at 37 °C, 5% CO_2 for 20 to 30 min. Right before imaging, OT-I T cells were dropped onto the coverslip which had the BMDCs. The sample was then loaded into the previously conditioned sample bath and secured. For imaging fixed cells, 5-mm round coverslips were cleaned by a plasma cleaner and coated with Cell-Tak with TetraSpeck fluorescent beads (0.1 μm at 1.8×10^8 beads per milliliter) at room temperature for 1 h and then washed with 18 MΩ water and dried. Fixed cells were dropped onto the coated coverslip and spun down at 1,400 × *g* for 10 min at 4 °C. The coverslip was then mounted on the microscope for imaging.

Imaging was performed with a 488-, 560-, or 642-nm laser (MPBC) dependent upon sample labeling in single- or two-color mode. Exposure time was 10 ms per frame, leading to a temporal resolution of 4.7 s in two-color mode.

Confocal Microscopy. Comparison confocal images were taken with an upright Leica Sp8 laser scanning confocal microscope equipped with a white-light laser, acoustooptical beam splitter, and five detectors including three photomultiplier tubes (PMTs) and two hybrid detectors (HyDs). The objective was a Leica HC PL APO 63×/1.20 water immersion objective. The images were collected in sequence between channels. Channel 1 was excited at 499 nm and collected with a HyD gain of 496 and a band pass of 504 to 755 nm. Channel 2 was excited at 653 nm and collected with a HyD gain of 318 and a band pass of 658 to 777 nm. Images were collected at 200-Hz unidirectional scan speed. The pinhole was optimized at 1 Airy Unit (AU) for 580-nm emission. Pixel/voxel size was 344 nm (*x*) × 344 nm (*y*) × 356 nm (*z*) with no digital zoom and 49 nm (*x*) × 49 nm (*y*) × 356 nm (*z*) for images with 7× digital zoom.

Deconvolution was performed using the Leica LAS X Lightning Deconvolution module using the "adaptive" strategy. Actual numbers of iterations were two for no digital zoom and three for 7× digital zoom. The refraction index was 1.33 for the water mounting medium.

Synaptic Cleft Mapping. The TIRF microscope was based on a Zeiss Axiovert 200M with a manual laser TIRF I slider. To image microvillar contacts and TCRs, image sequences consisting of TCRs (TIRF), QD-streptavidin (wide-field), and

interference reflection microscopy (IRM; wide-field) images were collected. For TIRF images, a 488-nm Obis laser (Coherent) was used for excitation of Alexa Fluor 488–labeled TCRs and a 640-nm laser was used for Alexa Fluor 647–labeled PD-1.

SCM used a combination of TIRF detection of TCR and PD-1 with wide-field excitation/emission of Qdots. Wide-field QD images were acquired using a 405/10× excitation filter (Chroma Technology) in a DG-4 xenon light source (Sutter). TCR and QD fluorescence were split using a DV2 with 565-nm long-pass dichroic and 520/35 m and 605/70 m emission filters (Photometrics). Split images were collected using an Evolve emCCD in quantitative mode (Photometrics). IRM images were acquired using a 635/20× excitation filter (Chroma Technology), and reflected light was collected onto the long-pass side of the DV2 imaging path. For a time-lapse image series, image sequences were typically acquired at 1- to 2-s intervals.

SCM-Based Contact Segmentation and Analysis. Contact detection has been described previously. Briefly, the IRM images were first filtered with a high-frequency emphasis filter, and then segmented using an active contour to identify the synapse footprint region on the bilayer. Intensity local minima inside the synapse region with intensities less than the median intensity in the synapse region were detected. Each local minimum was dilated with a three-pixel-diameter disk structuring element (a cross) and used as a mask input for active contour segmentation of the Qdot image. If the active contour failed to detect a region in the Qdot image, the contour collapsed and the minima were discarded. After independent segmentation of all regions, regions that shared >50% of their area were merged to produce a final segmentation. Pixel indices for identified contact regions that remained after active contour analysis were saved.

TIRF Contact TCR–PD-1 Colocalization. The contact TCR–PD-1 colocalization was performed using an in-house Matlab script. Briefly, the contact "footprints" were used as a mask to isolate fluorescence intensity associated with the TCR or PD-1. The intensity in each TCR or PD-1 "object" was then averaged and plotted in a histogram. A Gaussian distribution curve centered at the background fluorescence median was then overlayed. The contacts that fell within 3 sigma of the Gaussian distribution were then considered TCR^- or $PD\text{-}1^-$, while the higher-intensity contacts were considered TCR^+ or $PD\text{-}1^+$ and the binary representations were split into two separate image stacks.

LLSM: Postprocessing.

Deconvolution and channel-shift correction. Raw data were deconvolved utilizing the iterative Richardson–Lucy deconvolution process with a known point spread function that was recorded for each color prior to the experiment. The code for this process was provided by the Betzig laboratory at Janelia Farms. It was originally written in Matlab (MathWorks) and imported into CUDA (Nvidia) for parallel processing on the graphics processing unit (Nvidia, GeForce GTX Titan X). A typical sample area underwent 15 to 20 iterations of deconvolution.

Channel shifts between red and green channels were corrected using TetraSpeck beads embedded on the coverslip. Regions of interest (ROIs) within the sampling area were cropped down to size and compressed to 16-bit TIFFs using in-house Matlab code to allow immigration into Imaris (Bitplane) or UCSF ChimeraX (28) for visualization and further analysis.

Cluster detection and segmentation. Detection of clusters in images began by detecting the outer edge of cells using a custom program which applied a two-step *k* means clustering calculation on each image slice. Following the identification of the edge of the cell, the detected edge of the cell was such that the edge being analyzed had a thickness of 3 pixels. In order to locate the approximate positions of puncta, the exterior of the cell was subjected to a Pearson correlation calculation. In this step, a continuous set of small windowed 2D projections were created and a correlation calculation was conducted comparing these projections with a set of Gaussian kernels, each of different size. The correlation coefficients were then used in a custom clustering algorithm that applied a 3D watershed calculation to identify the edge and extent of specific clusters.

Patch size (area) calculation. To calculate the surface area of patches, the stack of images containing the patches were rendered as surfaces. The patch information was then added to the nodes (instead of intensity) after the initial creation of the surface. In a surface, there are many small triangles that comprise the surface. We then find all of the triangles (surface elements) that comprise a patch. The area of each triangle is half the magnitude of the cross product of the vectors that define the triangle. For a patch, we find the area of the constituent triangles and sum them to define the area of the patch.

Calculation of the size of a diffraction-limited object. To determine the size of a diffraction-limited object, images of diffraction-limited beads were collected in three dimensions with LLSM. In this procedure, we began by taking *xz* projections of these beads, which gives a "side-on" view of the bead showing what the bead would look like if you were standing on the *xy* plane and looking at the bead. Each one of the intensities of the bead in this side-on view projection has associated *xz* coordinates which we also determined. The intensities and the associated *xz* coordinates from this projection of the bead were then mapped onto a 3D surface of a T cell which was made to have a homogeneous intensity initially. In this process, nodes on the intensity surface rendering of the T cell were replaced with the intensities from two dimensions (side-on projection) of the bead along the same *xz* coordinates of the side-on projection of the bead. In other words, the intensities of the bead were moved to the surface of the cell to match as close to 1:1 as possible the *xz* coordinates of the side-on projection of the bead. In this way, we could see what the axial size of the bead would be on a surface rendering of the cell. Note that the size of the beads in their *xz* projection on the surface of the cell was very close, as expected, to the size of the beads themselves.

Therefore, by projecting axially onto the surface of the T cell, the image of a bead was added to the 3D T cell surface. When adding the bead onto the cell surface, we made a cluster. We then added the bead to different locations on the T cell surface and calculated the surface area of the resulting clusters (the projected beads). The surface area was calculated using the surface rendering (not intensity stack). Every element of the surface is a series of three nodes that make up a triangle. Many of these triangles make up the surface. We found all the triangles associated with the bead (cluster) and computed their surface area. The area of each triangle is defined as half the magnitude of the cross product of the vectors that define the triangle.

Defining the region of a microvillus. The threshold of the curvature used to define the microvilli is applied in order to eliminate regions that are valley-like. The curvature is calculated on an absolute scale across all cells where positive values define valley-like features and negative values define peak-like structures. To define microvilli, the maximum of the curvature threshold was set to −0.05, in order to encapsulate peak-like structures down to their base while not capturing any valley-like components. This threshold was determined by examining multiple sets in order to determine a correct absolute threshold that defines the microvillus without cropping it and without including any neighboring valley-like features in the definition of the microvillus. Once the thresholded curvature surface is defined, this information is sent to our custom Matlab program that defines the microvilli. The program begins by finding all the local peaks in the curvature surface. Once these peaks are identified, the program then uses a combination of watershedding and overlap calculation to individually identify each microvillus. The final output of the code is a list of *xyz* coordinates of the nodes on the surface along with a corresponding list of villi numbers.

Cluster colocalization analysis. Colocalization analysis began by registering the images collected in the green and red channels. In this step, any section of a boundary located in the red channel and the green channel which was within a radial distance of 3 pixels was considered to be the same. A voxel-based colocalization calculation was then done which identified the voxels and clusters which overlapped in the green and red channels. Finally, a blob analysis yielded sets of colocalizing clusters occupying similar shapes on the exteriors of the images of cells. All algorithms for identifying clusters and calculations with colocalization were written in Matlab (MathWorks).

Defining the fraction of TCRs in patches. An ROI was cropped tightly to the isolated cell area, and total TCR fluorescence intensity of that region was used to define the whole-cell integrated intensity. To define the thresholded patch integrated intensity, all TCR intensity values below 120 AU were set to 0 to define a consistent threshold across all samples for defining areas of high fluorescence intensity. Surfaces were then created based on thresholded data, and TCR fluorescence intensity within those surfaces was summed to get the thresholded patch integrated intensity.

Receptor patch tracking. Tracking of receptor patches and microvilli was performed in Imaris 9 (Bitplane). After deconvolution and channel-shift correction, TIFF files were imported into Imaris. Spot functions with tracking were used to detect and track patches. The resulting tracks were manually cleaned to only show the tracks on the cell surface. Mean track speed was calculated using the

built-in functions in Imaris. Specific values of tracks were exported to be further analyzed. MSD calculation and fitting were performed in Matlab using the package msdanalyzer (29).

Statistical Information. Statistical details of experiments can be found in the figure legends with exact *P* values. The *P* values are indicated in the figures when $P < 0.05$. Welch's *t* test and paired *t* test were performed in Prism 9 (GraphPad) software. Mean SD and SEM (SE) were determined using Matlab (MathWorks) or Prism 8 or 9 (GraphPad) software.

Data Availability. All code for data analysis associated with this article has been deposited in GitHub (https://github.com/BIDCatUCSF). Imaging data are available upon request.

ACKNOWLEDGMENTS. We thank members of the M.F.K. lab for discussions and Erron Titus for critical reading. This work was supported by NIH Grant AI052116 (to M.F.K.) and Cancer Research Institute Irvington/Robertson (United States) postdoctoral fellowships (to E.C.).

1. M. M. Davis *et al.*, T cells as a self-referential, sensory organ. *Annu. Rev. Immunol.* **25**, 681–695 (2007).
2. P. A. van der Merwe, O. Dushek, Mechanisms for T cell receptor triggering. *Nat. Rev. Immunol.* **11**, 47–55 (2011).
3. A. Grakoui *et al.*, The immunological synapse: A molecular machine controlling T cell activation. *Science* **285**, 221–227 (1999).
4. D. R. Fooksman *et al.*, Functional anatomy of T cell activation and synapse formation. *Annu. Rev. Immunol.* **28**, 79–105 (2010).
5. A. Gérard *et al.*, Detection of rare antigen-presenting cells through T cell-intrinsic meandering motility, mediated by Myo1g. *Cell* **158**, 492–505 (2014).
6. E. Cai *et al.*, Visualizing dynamic microvillar search and stabilization during ligand detection by T cells. *Science* **356**, eaal3118 (2017).
7. G. Campi, R. Varma, M. L. Dustin, Actin and agonist MHC-peptide complex-dependent T cell receptor microclusters as scaffolds for signaling. *J. Exp. Med.* **202**, 1031–1036 (2005).
8. T. Yokosuka *et al.*, Newly generated T cell receptor microclusters initiate and sustain T cell activation by recruitment of Zap70 and SLP-76. *Nat. Immunol.* **6**, 1253–1262 (2005).
9. K. Choudhuri, D. Wiseman, M. H. Brown, K. Gould, P. A. van der Merwe, T-cell receptor triggering is critically dependent on the dimensions of its peptide-MHC ligand. *Nature* **436**, 578–582 (2005).
10. S. J. Davis, P. A. van der Merwe, The kinetic-segregation model: TCR triggering and beyond. *Nat. Immunol.* **7**, 803–809 (2006).
11. K. Y. Chen *et al.*, Trapping or slowing the diffusion of T cell receptors at close contacts initiates T cell signaling. *Proc. Natl. Acad. Sci. U.S.A.* **118**, e2024250118 (2021).
12. D. S. Lyons *et al.*, A TCR binds to antagonist ligands with lower affinities and faster dissociation rates than to agonists. *Immunity* **5**, 53–61 (1996).
13. I. Stefanová *et al.*, TCR ligand discrimination is enforced by competing ERK positive and SHP-1 negative feedback pathways. *Nat. Immunol.* **4**, 248–254 (2003).
14. B. F. Lillemeier, J. R. Pfeiffer, Z. Surviladze, B. S. Wilson, M. M. Davis, Plasma membrane-associated proteins are clustered into islands attached to the cytoskeleton. *Proc. Natl. Acad. Sci. U.S.A.* **103**, 18992–18997 (2006).
15. C. Wülfing *et al.*, Costimulation and endogenous MHC ligands contribute to T cell recognition. *Nat. Immunol.* **3**, 42–47 (2002).
16. C. R. Glassman, H. L. Parrish, M. S. Lee, M. S. Kuhns, Reciprocal TCR-CD3 and CD4 engagement of a nucleating pMHCII stabilizes a functional receptor macrocomplex. *Cell Rep.* **22**, 1263–1275 (2018).
17. J. M. Turner *et al.*, Interaction of the unique N-terminal region of tyrosine kinase p56lck with cytoplasmic domains of CD4 and CD8 is mediated by cysteine motifs. *Cell* **60**, 755–765 (1990).
18. C. Wülfing, M. D. Sjaastad, M. M. Davis, Visualizing the dynamics of T cell activation: Intracellular adhesion molecule 1 migrates rapidly to the T cell/B cell interface and acts to sustain calcium levels. *Proc. Natl. Acad. Sci. U.S.A.* **95**, 6302–6307 (1998).
19. B. T. Fife, J. A. Bluestone, Control of peripheral T-cell tolerance and autoimmunity via the CTLA-4 and PD-1 pathways. *Immunol. Rev.* **224**, 166–182 (2008).
20. B. C. Chen *et al.*, Lattice light-sheet microscopy: Imaging molecules to embryos at high spatiotemporal resolution. *Science* **346**, 1257998 (2014).
21. S. Ghosh *et al.*, ERM-dependent assembly of T cell receptor signaling and co-stimulatory molecules on microvilli prior to activation. *Cell Rep.* **30**, 3434–3447.e6 (2020).
22. U. H. von Andrian, S. R. Hasslen, R. D. Nelson, S. L. Erlandsen, E. C. Butcher, A central role for microvillous receptor presentation in leukocyte adhesion under flow. *Cell* **82**, 989–999 (1995).
23. Y. Jung *et al.*, Three-dimensional localization of T-cell receptors in relation to microvilli using a combination of superresolution microscopies. *Proc. Natl. Acad. Sci. U.S.A.* **113**, E5916–E5924 (2016).
24. T. Yokosuka *et al.*, Programmed cell death 1 forms negative costimulatory microclusters that directly inhibit T cell receptor signaling by recruiting phosphatase SHP2. *J. Exp. Med.* **209**, 1201–1217 (2012).
25. A. Cambi *et al.*, Organization of the integrin LFA-1 in nanoclusters regulates its activity. *Mol. Biol. Cell* **17**, 4270–4281 (2006).
26. Y. Zhang, H. Wang, Integrin signalling and function in immune cells. *Immunology* **135**, 268–275 (2012).
27. P. Beemiller, J. Jacobelli, M. F. Krummel, Integration of the movement of signaling microclusters with cellular motility in immunological synapses. *Nat Immunol.* **13**, 787–795 (2012).
28. E. F. Pettersen *et al.*, UCSF ChimeraX: Structure visualization for researchers, educators, and developers. *Protein Sci.* **30**, 70–82 (2021).
29. N. Tarantino *et al.*, TNF and IL-1 exhibit distinct ubiquitin requirements for inducing NEMO-IKK supramolecular structures. *J. Cell Biol.* **204**, 231–245 (2014).